Remote Sensing of Environment 218 (2018) 221–230

Contents lists available at ScienceDirect

Remote Sensing of Environment

journal homepage: www.elsevier.com/locate/rse

Deformation of Linfen-Yuncheng Basin (China) and its mechanisms revealed by II-RATE InSAR technique

Chaoying Zhao[a,b,*], Chuanjin Liu[a,c], Qin Zhang[a,b], Zhong Lu[d], Chengsheng Yang[a,b]

[a] School of Geology Engineering and Geomatics, Chang'an University, No.126 Yanta Road, Xi'an 710054, China
[b] National Administration of Surveying, Mapping and Geoinformation, Engineering Research Center of National Geographic Conditions Monitoring, Xi'an 710054, China
[c] The Second Monitoring and Application Center, China Earthquake Administration, Xi'an 710054, China
[d] Huffington Department of Earth Sciences, Southern Methodist University, Dallas, TX 75275, USA

ARTICLE INFO

Keywords:
InSAR
Fault
Subsidence
Ground fissure
Deformation
Linfen-Yuncheng Basin (LYB)
Poly-interferogram rate and time-series estimator algorithm (II-RATE)

ABSTRACT

The Linfen-Yuncheng Basin (LYB) in China is a region possessing severe geo-hazards, including active tectonic fault movement, land subsidence and ground fissures among others. Interferometric Synthetic Aperture Radar (InSAR) technique is applied to map surface deformation associated with various geo-hazards in this basin. The poly-interferogram rate and time-series estimator algorithm (II-RATE) is used over forty-nine scenes of SAR data to generate the deformation maps over the entire LYB. The precision of InSAR results is around 3 mm/yr. Some active faults and ground fissures are successfully detected. The spatiotemporal characteristics of tableland uplift, faults displacement and basin subsidence are quantitatively monitored with InSAR technique ranging from 2 mm/yr to 142 mm/yr. Finally, the mechanisms of surface deformation regarding large scale Zhongtiaoshan fault, middle scale basin land subsidence and small scale ground fissures are discussed in terms of interseismic movement, underground water level changes and hydrostratigraphic heterogeneity.

1. Introduction

The Linfen-Yuncheng Basin (LYB) is located in the south-central Shanxi graben system, where the tectonic formation is extremely complex with frequent seismic events (Liu and Ji, 2014; Wang, 1995) (Fig. 1). Historically, more than ten earthquakes with magnitude (M) larger than 7.0 have occurred in this basin, including the M 8 Hongtong earthquake in 1303 and M 7.5 Linfen earthquake in 1695. The most recent significant earthquake was an M 4.4 event near Yuncheng on Mar. 12, 2016. Two large-scale piedmont normal faults control LYB, namely the Luoyunshan fault (LYF) to the northwest and the Zhongtiaoshan fault (ZTF) to the southeast. These faults slip at a rate as large as 2 mm/yr, as monitored by campaign leveling and GPS measurements (Hao et al., 2016; Cui et al., 2016). While, long-term inter-seismic movement estimated by radiocarbon (^{14}C) dating has shown the mean slip rate of the Northern ZTF is 0.75 ± 0.05 mm/a since 24.7 ka BP (Si et al., 2014), no quantitative measurement has been done on small and secondary normal faults, which strike mainly to the northeast-east and east-west within the LYB. Little is known about buried faults in the region. In addition, four large historical land subsidence areas have been recorded in LYB: Yaodu district at Linfen, Jishan County, Taocun-Xiaxian, and Hejin (Yang et al., 2016). The first three areas are also superimposed by clusters of ground fissures, and Hejin is suffering from abnormal surface subsidence and uplift (Yang et al., 2016; Ji et al., 2016). So, how can basin-scale deformation be efficiently and precisely monitored? Is it possible to separate different hazard deformation fields from each other? And what are the mechanisms of the complex hazards in LYB? These are the research questions that we attempt to address in this paper.

Conventional ground-based geodetic techniques, such as GPS and leveling, have been applied to monitor the fault movements in LYB (Hao et al., 2016; Liu et al., 2016; Cui et al., 2016). However it is difficult to detect detailed and comprehensive ground deformation due to their low spatial resolution. In contrast, InSAR can provide surface deformation measurement at meter-scale spatial resolution. Preliminary results of the land subsidence in LYB during 2008–2010 have been previously reported (Yang et al., 2016). This research addressed several challenges in applying InSAR techniques, such as decorrelation in the farmland and mountainous regions, and tropospheric delay artefacts. In addition, data from both C-band Envisat and L-band ALOS-1 PALSAR were exploited to enhance deformation measurements. So, this research is fourfold: (i) large coverage surface deformation mapping using multi-frame, multi-track SAR data, (ii) comparison of InSAR results from multiple sensors with different headings, looking angles and

* Corresponding author at: School of Geology Engineering and Geomatics, Chang'an University, No.126 Yanta Road, Xi'an 710054, China
E-mail address: cyzhao@chd.edu.cn (C. Zhao).

https://doi.org/10.1016/j.rse.2018.09.021
Received 7 August 2017; Received in revised form 23 August 2018; Accepted 24 September 2018

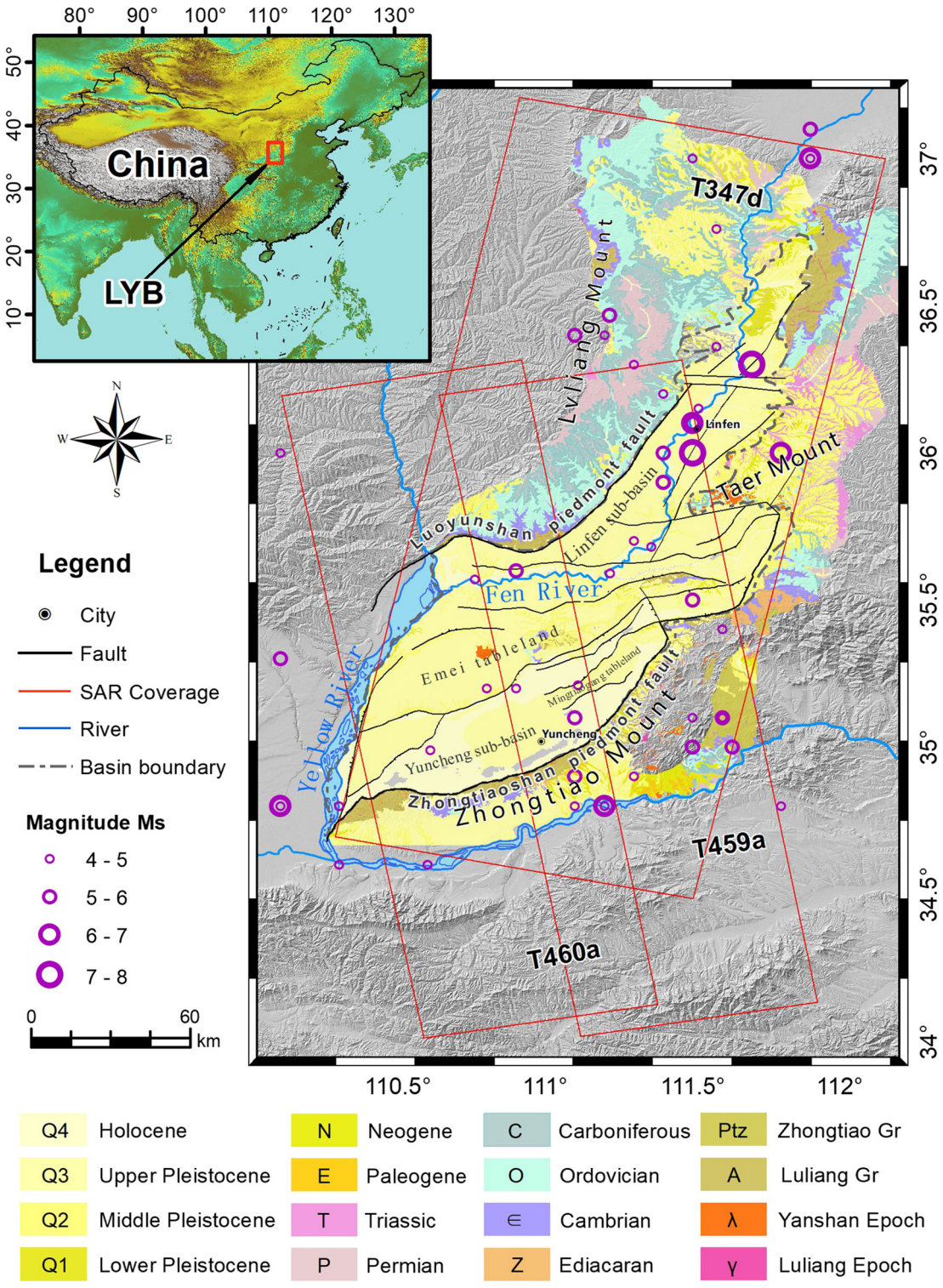

Fig. 1. Shaded relief Map of the Linfen-Yuncheng Basin (LYB). Red polygons show the coverage of the three SAR tracks, grey dashed line outlines the area of LYB, and black lines show the active normal faults. The epicenters of earthquakes with magnitude greater than M 4 that occurred from 1831 BCE to 2016 are shown with purple circles. The inset shows the location of LYB. (For interpretation of the references to colour in this figure legend, the reader is referred to the web version of this article.)

wavelengths, (iii) InSAR results from different tracks and sensors were then merged for basin-wide deformation analysis of the entire LYB by considering the relative offsets in the overlapped regions and the absolute offsets, as determined by leveling and GPS measurements, and (iv) interpretation of the mechanisms of different deformation fields within the LYB at a variety of spatial scales.

2. Geological setting

2.1. Geomorphology

In Fig. 1, LYB is bounded by the Lvliang Mount to the northeast and the Zhongtiao Mount to the southwest. Taer Mount, Emei tableland,

Mingtiaogang tableland are located in the center of LYB. Fen River, a large branch of the Yellow River, goes through the basin and merges into the main stream of the Yellow River to the west of the basin.

2.2. Quaternary deposits

The quaternary deposits in LYB are as thick as 490 m, composed of four series: lower Pleistocene (Q1), middle Pleistocene (Q2), upper Pleistocene (Q3) and Holocene (Q4). The sedimentary thicknesses for these four series range from 10 to 400 m, 45 to 202 m, 3 to 65 m, and 0 to 20 m, respectively. In each series, the sedimentary thickness varies greatly from the edges to the center of the basin.

2.3. Faults

Three kinds of tectonic faults exist in LYB according to the characteristics and spatial scales, including major piedmont faults at the edges of the basin, boundary faults within the basin between different geomorphology units, and some hidden faults. As shown in Fig. 1, the major piedmont faults include the 120-km-long LYF, bounding the north of the LYB along a NNE direction, and the 137-km-long ZTF bounding the south of the LYB with a similar distribution trend to the LYF. These two major faults can be divided further into 5 and 3 sections, respectively, according to the variations in strike, dip angle, slip rate etc. The Huoshan piedmont fault with NS trend and 60 km in length is located in the Linfen sub-basin (Fig. 1). Two tableland faults include the North Emei fault (NEF) and South Emei fault (SEF). These faults represent the south boundary of Linfen sub-basin and the north boundary of Yuncheng sub-basin. The lengths of these two faults are 85 km and 130 km, and the trends are NEE and NEE ~ NE, respectively. In addition, five faults with lengths ranging from 30 to 50 km are distributed within the Linfen sub-basin; these faults delimitate the small-scale grabens and tablelands within the sub-basin. Finally, the LYB contains many hidden faults, including 27 that can be inferred in the Linfen sub-basin and another 8 in the Yuncheng sub-basin (Meng, 2011). This indicates the Linfen sub-basin is more tectonically complex than the Yuncheng sub-basin.

3. SAR data and interferogram formation

To monitor the surface deformation in the LYB, archived SAR imagery data acquired from 2007 to 2011, including C-band Envisat/ASAR data by the European Space Agency (ESA) and L-band ALOS/PALSAR data acquired by JAXA were processed. Firstly, spatial baseline thresholds for Envisat and ALOS data were 500 m and 2000 m, respectively. And temporal baseline for Envisat data was 470 days, but no temporal baseline for ALOS data was set. In total forty-nine scenes SAR data along three tracks were selected to generate interferograms: 8 scenes of descending Envisat images on track 347, 21 scenes of ascending ALOS images from track 459, and 20 ascending ALOS images from track 460. Table 1 includes the imaging parameters of different SAR images. Track locations are illustrated with red polygons on Fig. 1.

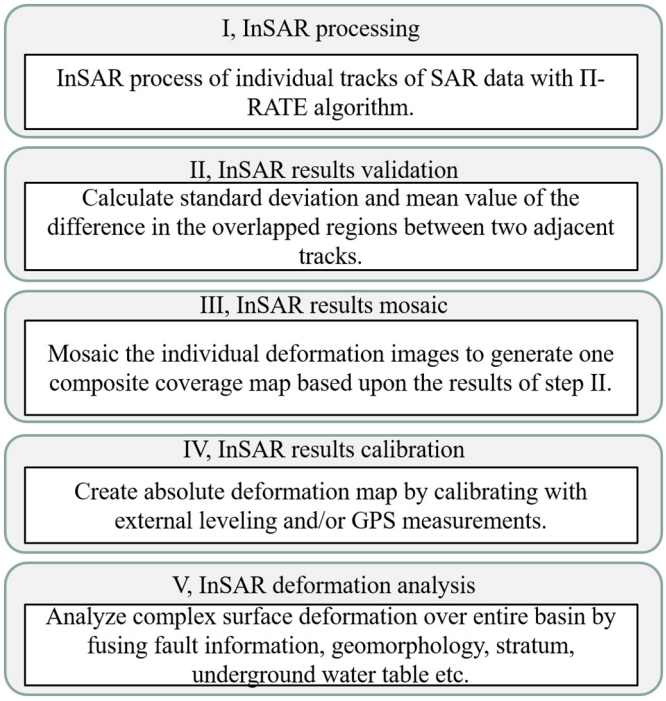

Fig. 2. Flowchart of different scale deformation analysis with Π-RATE InSAR method.

Interferograms are routinely processed using GAMMA InSAR software. To improve the coherence, a big multi-looking number was set for Envisat and ALOS data to obtain a final pixel size as large as 80 m, respectively. Topographic effect in the interferograms was removed using a 30-m Shuttle Radar Topography Mission Digital Elevation Model (SRTM DEM) (Farr et al., 2007).

4. Methodology

In order to accurately map the absolute deformation field over multi-tracks SAR data coverage region, the poly-interferogram rate and time-series estimator algorithm (Π-RATE) was firstly applied for each individual SAR data. Then InSAR results from different tracks and sensors were merged for basin-wide deformation analysis of the entire LYB by considering the relative offsets in the overlapped regions and the absolute offsets, as determined by leveling and GPS measurements. Lastly, different spatial scales of surface deformation were determined from InSAR results, including large-scale fault movement, medium-scale land subsidence and small-scale ground fissures. The process flowchart is shown in Fig. 2.

Π-RATE employs a pixel-wise approach to calculate deformation rates at pixels that are coherent in different numbers of interferograms, thus ensuring that useful information about the magnitude and spatial extent of the deformation field can be retrieved. This method originated

Table 1
SAR data and their imaging parameters.

Satellite/sensor	ENVISAT/ASAR	ALOS/PALSAR	
Band	C	L	
Wavelength (mm)	56.6	236.1	
Polarization	VV	HH	
Repeat time (d)	35	46	
Track	347	459	460
Heading (°)	−168.0	−10.2	−10.2
Incidence angle (°)	22.8	38.7	38.7
scenes	8	21	20
Time span (yyyymmdd)	20090220–20101008	20061222–20110102	20070108–20110119

from the multi-interferogram method proposed by Biggs (Biggs et al., 2007). Then Wang (Wang et al., 2012) improved this method and produced a rate map showing the average displacement rate of each pixel, as well as a time series of displacement. This technique has been successfully used in Tibet (Garthwaite et al., 2013; Wang and Wright, 2012), Turkey (Walters et al., 2014) and Medicine Lake Volcano (Parker et al., 2014).

The Π-RATE method uses a network-based approach on the geocoded interferograms to calculate the noise contribution at each acquisition, rather than at each interferogram, such as orbital and atmospheric delay errors (Biggs et al., 2007; Elliott et al., 2008; Wang et al., 2009). Atmospheric phase screen (APS) filtering is applied to mitigate atmospheric disturbances: a temporal high-pass filter followed by a spatial low-pass filter similar to the PS algorithm (Ferretti et al., 2001). Here we use a Gaussian temporal filter of $1\sigma = 0.5$ years to minimize temporal variations shorter than one year as we focus on long-term, steady velocities. We apply a Butterworth spatial filter and estimate the variance and covariance using a best fit 1-D covariance function (Hanssen, 2001).

Finally, a weighted least squares inversion is used to determine the best-fitting rate and associated root mean square (RMS) misfit to the interferograms on a pixel-by-pixel basis, using a variance-covariance matrix (VCM) to account for the spatial and temporal correlation between interferograms (Wang et al., 2012). Pixels that are not coherent for at least a set number of coherent observations (between 5 and 8) are deemed unreliable and excluded from the deformation rate maps. We then calculate the ratio of RMS misfit and its associated a-priori standard deviation from the VCM. If any ratio is greater than a given threshold, the observation with the maximum ratio is removed and the rate is re-evaluated with one less observation. This continues until all interferograms have residuals less than 3 times of their standard deviations, or there are less than 5–8 interferograms remaining for that pixel. We have also removed pixels with RMS misfits larger than a priori value, e.g. 3–4 mm/yr.

The displacement rates (V) and their uncertainties (R) are given by Eqs. (1) and (2) in a least squares sense.

$$V = [T^T\Sigma^{-1}T]^{-1}T^T\Sigma\Phi \quad (1)$$

$$R = [T^T\Sigma^{-1}T]^{-1} \quad (2)$$

where $\boldsymbol{\Phi}$ is the interferometric displacement observations, T indicates the interferogram time spans, Σ is the VCM.

5. Validation of InSAR results

5.1. Validation of InSAR results

Π-RATE InSAR results for three tracks SAR data shown in Table 1 and Fig. 1 are shown in Fig. 3. As GPS measurements (Hao et al., 2016; Cui et al., 2016) and previous Envisat analysis (Yang et al., 2016) suggested that no significant horizontal deformation within the LYB, Fig. 3 shows the annual vertical deformation maps considering respective satellite look angles.

It is clear to see from Fig. 3 that L-band ALOS data (tracks 459 and 460) can generally provide more coherent pixels than C-band Envisat data (track 347) for the same monitoring area during the similar data coverage period in the study region. Meanwhile, Π-RATE InSAR method can provide entirely consistent results for ALOS and Envisat data, despite some differences in detailed characteristics.

In order to quantitatively assess the precision of deformation results obtained by Π-RATE InSAR technique, results from multiple sensor data with different satellite flight directions, looking angles and even wavelengths were evaluated. Fig. 4(a) and (b) shows the histograms of vertical deformation difference within the overlapped region between two adjacent SAR data tracks. Fig. 4(a) shows the results between ALOS tracks 459 and 460, while Fig. 4(b) shows the results between ascending ALOS and descending Envisat data.

Standard deviations calculated in the overlapped regions from two independent SAR datasets illustrate the inner precision of InSAR techniques, we conclude that the precision of Π-RATE method is better than 3 mm/yr (i.e. $4.2/\sqrt{2}$ for ascending and descending comparison).

5.2. Calibration of InSAR results

A basin-wide LYB deformation map was generated by fusing the individual results from the three independent SAR tracks. Offsets calculated from overlapped regions shown in Fig. 4(a) and (b) were considered to merge results. Exactly to say, the average is calculated if a pixel is observed in two tracks, and it will be kept if it is only observed in one track. Next, the absolute vertical deformation result was validated with external leveling and GPS measurements. Firstly, root mean square errors are calculated with the difference between InSAR and GPS and leveling measurements, which are 3.4 mm/y and 4.3 mm/y, respectively. Then outliers are determined if they are larger than two times of root mean square errors. As a result, 155 out of 199 leveling points and 54 out of 70 GPS points are left over LYB in calculating the absolute shift of InSAR results and the root mean square error (RMSE) (Cui et al., 2016). The regression functions between InSAR and leveling, and between InSAR and GPS results are shown in Eqs. (3) and (4), respectively.

$$Y = 0.99315\,X + 0.03606 \quad (3)$$

$$Y = 0.98481\,X + 1.92374 \quad (4)$$

The correlation coefficients between InSAR and leveling and between InSAR and GPS reach 0.77 and 0.92, respectively. The scatter diagrams between InSAR, leveling and GPS are shown in Fig. 4(c) and (d). The deformation range of leveling measurements are much smaller than the GPS one, and if the maximum and minimum GPS points are deleted, the correlation coefficient between GPS and InSAR results will be decreased to 0.67. Moreover, as leveling has higher precision than GPS vertical component measurement, the entire InSAR deformation map was calibrated with only leveling measurements. Finally, the absolute InSAR results over entire LYB is obtained shown in Fig. 5. The RMSE of InSAR result after calibration is around 2.9 mm/yr, which indicates the accuracy of Π-RATE InSAR measurement in this study.

6. Results analysis

The surface deformation fields of LYB, including displacements from active and buried faults, long-term slow-rate tableland and basin displacement, severe land subsidence, temporal uplift, and deformation associated with ground fissures deformation, are all discussed. In addition, based on the composite basin-wide LYB annual vertical deformation rate map, small-scale time-series deformation maps along leveling and GPS profile lines are analyzed to uncover additional features.

6.1. Fault displacement

Leveling and GPS have been employed in this region from 1994 to 2014 and from 2009 to 2015, respectively to detect the long term and slow rate range-basin scale deformation (Hao et al., 2016, 2014; Cui et al., 2016). As shown in Fig. 5, four profiles using leveling and GPS measurements are compared to Π-RATE InSAR results: AA′ uses both leveling and GPS, BB′ uses leveling, CC′ uses GPS measurements, and DD′ uses leveling. Results of the comparison appear in panels (a)–(d) of Fig. 6, where locations of faults are indicated with grey columns, and topography is shown on the bottom in each panel.

LYF is an active long fault controlling the northeastern boundary of the LYB. The uplift and subsidence rates along profile AA′ (Fig. 6(a)) in the foot wall and the hanging wall are around 2 mm/yr and 1 mm/yr,

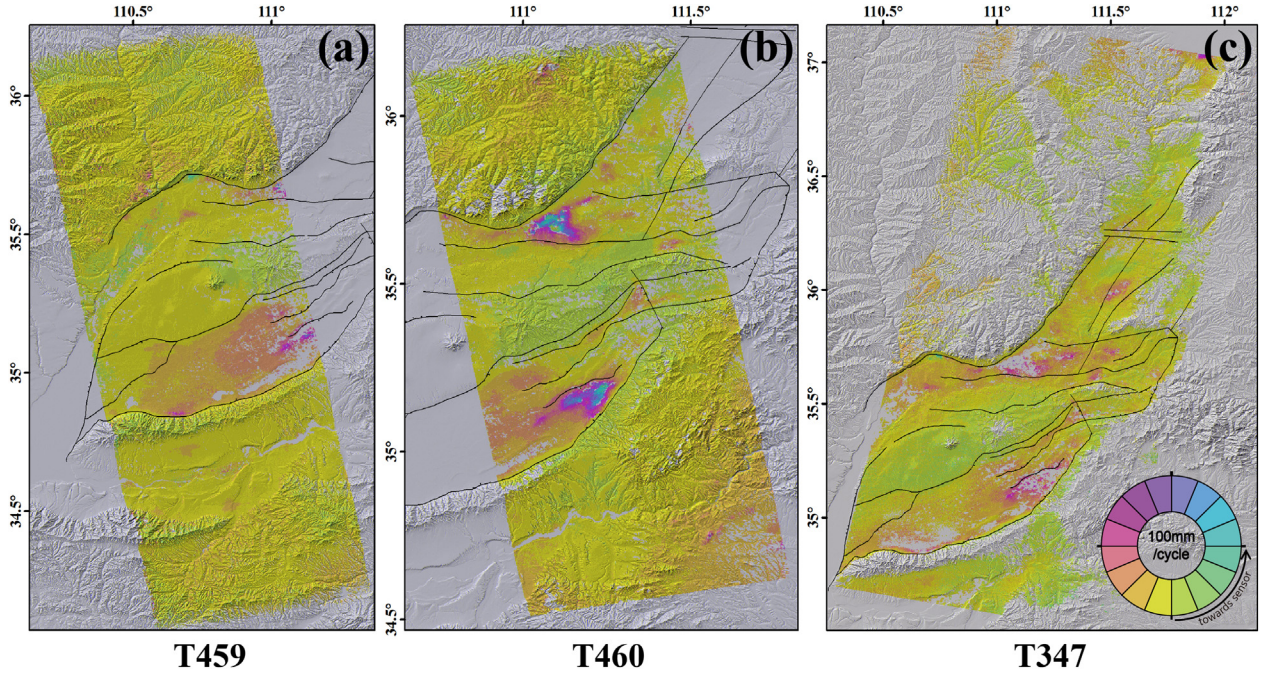

Fig. 3. Annual vertical deformation maps generated by Π-RATE InSAR technique. (a) Tracks 459 and (b) 460 indicate ascending data of ALOS/PALSAR and (c) Track 347 indicates descending Envisat/ASAR. Track coverages are shown in Fig. 1. And the maximum annual deformation is 100 mm/yr. (For interpretation of the references to colour in this figure legend, the reader is referred to the web version of this article.)

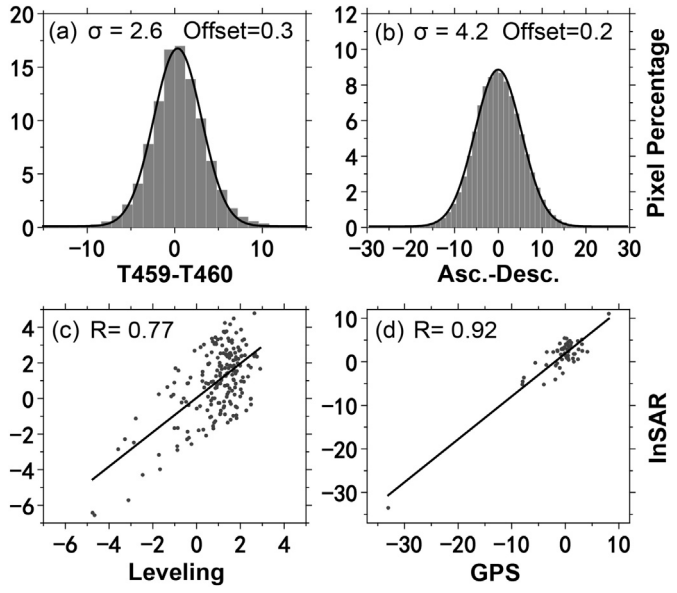

Fig. 4. InSAR accuracy assessment results. (a) Histogram, standard deviation (σ), and relative offsets of InSAR differences between two adjacent ascending ALOS SAR data tracks and (b) 2 ascending ALOS SAR data tracks versus 1 descending Envisat data tracks, Y axis is pixel percentage in the overlay region and x axis is rate difference. (c) Scatter diagram between Π-RATE InSAR results and leveling results and (d) between Π-RATE results and GPS results, the correlation coefficients between InSAR and leveling and between InSAR and GPS are shown in each panel.

respectively, which match well with leveling results. However, due to the few GPS benchmarks and low vertical monitoring precision relative to leveling measurement, the GPS results show less than 1 mm/yr uplift and 1 mm/yr subsidence along profile AA′, respectively. However, both leveling and GPS have similar deformation trends, except the points in the abnormal deformation region, the north of Hejin county.

Both profiles BB′ (Fig. 6(b)) and CC′ (Fig. 6(c)) monitor the displacement of southern Emei tableland fault (SEF), in which both leveling and InSAR results have high consistency along profile BB′, showing that the uplift and subsidence of Emei tableland and Yuncheng sub-basin along this profile are 1.8 mm/yr and1.5 mm/yr, respectively. In addition, GPS and InSAR have similar deformation pattern along profile CC′, where the uplift of Emei tableland and the subsidence of Yuncheng sub-basin along this profile are 1.5 mm/yr and 8 mm/yr, respectively. Then, from the profile DD′ (Fig. 6(d)), the uplift of Mingtiaogang tableland between north Mingtiaogang fault (NMF) and south Mingtiaogang fault (SMF) can be monitored by InSAR results is less than 1 mm/yr, while only one leveling point shows no obvious deformation, which indicates that Mingtiaogang tableland is stable during this period. However, to the north and to the south of Mingtiaogang tableland, two land subsidence regions can be clearly detected with both leveling and InSAR results. Lastly, as for another main controlling fault to the south of LYB, i.e. the Zhongtiaoshan piedmont fault (ZTF), all GPS, leveling and InSAR results show highly consistent results, which indicate the uplift of the Zhongtiao Mount is at the rate as large as 2 mm/yr. Fig. 6(e) shows the deformation of five active faults in the LYB along profile EE′: LYF, Jishan-Quwo fault (JQF), NEF, SEF and ZTF. The uplift shown on Fig. 6(e) to the north of LYF, from NEF to SEF, and to the south of ZTF correspond respectively to the uplift of Luoyun Mount (the southern section of Lvliang Mount), the Emei tableland, and Zhongtiao Mount. Two subsidence cones are correlated with relatively lower underground water levels, particularly between SMF and ZTF, where several ground fissures (Meng, 2011) can be detected over the subsidence bowls.

In summary, three tablelands, namely Luoyun Mount to the north, Emei tableland in the center and Zhongtiao Mount to the south of LYB are all displaying uplift with a magnitude of 2 mm/yr, 1.8 mm/yr and 2 mm/yr, respectively. And five faults, namely LYF, JQF, NEF, SEF and ZTF are active during this monitoring period.

6.2. Land subsidence due to ground water extraction

As shown with the pink and purple shading on Fig. 5, Yaodu, Jishan, Hejin in Linfen sub-basin, and the entire Yuncheng sub-basin suffer

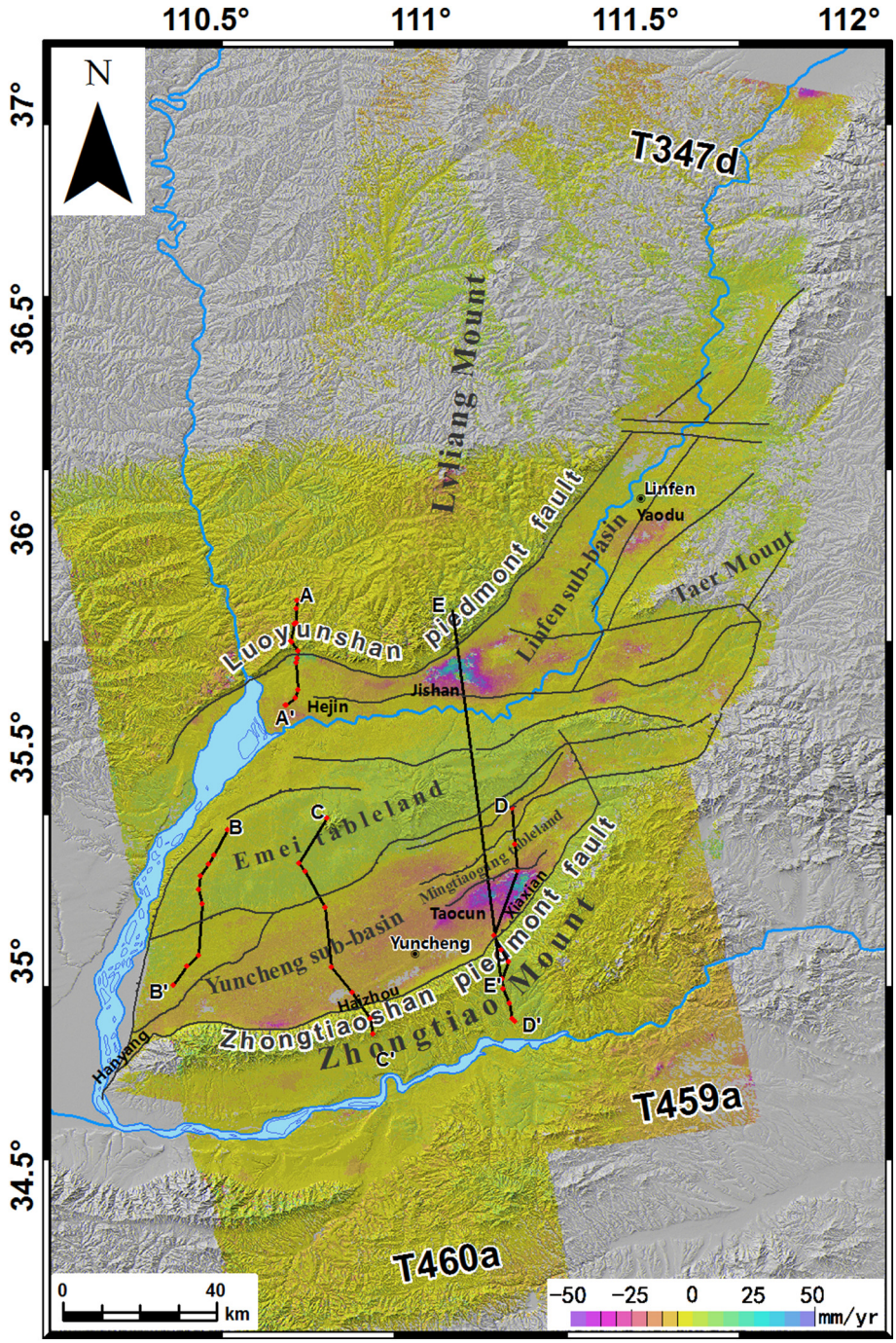

Fig. 5. Entire LYB vertical deformation rate map from the year of 2006 to 2011 generated with Π-RATE InSAR technique, where profiles AA′, BB′ and DD′ are leveling routes, profile CC′ is the connection of GPS benchmarks, and profile EE′ is the profile to show InSAR deformation and underground water depth in Fig. 6. (For interpretation of the references to colour in this figure legend, the reader is referred to the web version of this article.)

severe land subsidence. The total land subsidence area amounts to 2690 km^2. The maximum subsidence rate reaches 142 mm/yr in Jishan of Linfen sub-basin and 104 mm/yr in Taocun-Xiaxian of Yuncheng sub-basin. In addition, most land subsidence funnels are controlled by two normal faults with opposite slip angles. The main land subsidence funnels elongate along the direction parallel to the strike of the local faults.

As seen on profile EE′ in Fig. 6(e), two large land subsidence cones are correlated to the drawdown in underground water level, which Meng (2011) explained as the main cause of land subsidence in LYB.

6.3. Ground fissure detection

The enlarged deformation maps over two triangular regions, i.e. Jishan County in Linfen sub-basin and Xiaxian County in Yuncheng sub-basin are shown in Fig. 7(a) and (b), respectively, where faults and local fissures are superimposed.

From Fig. 7, ground fissures are controlled mainly by the local faults, and were located on the downthrown side, i.e. hanging wall of a normal fault. Most ground fissures rupture to the surface at the sections with a large deformation gradient (Fig. 7). Hence based on the gradient deformation map, ground fissures can be possibly detected. All fissures detected in the field are mapped in Fig. 7(a) and (b), on which some

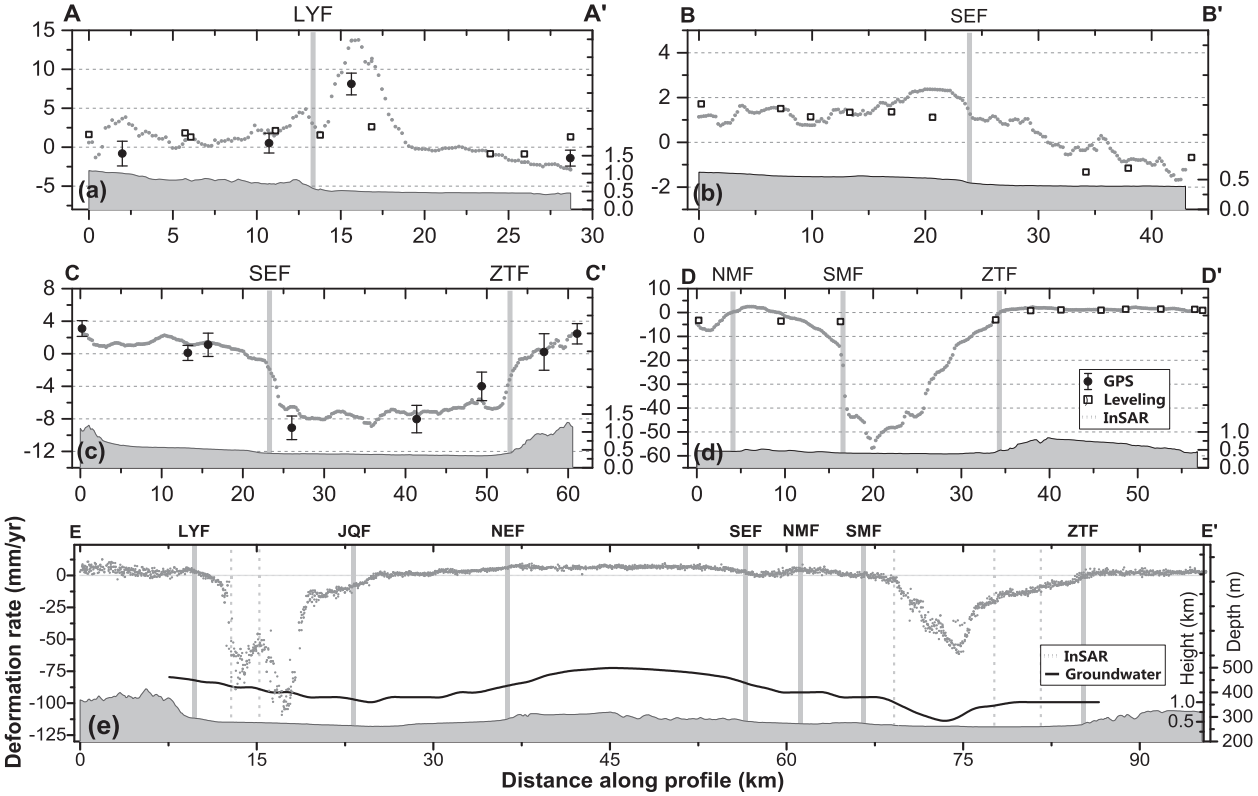

Fig. 6. Profiles of InSAR results generated from II-RATE method, on which leveling and/or GPS measurements are superimposed, error bar shows GPS precision with one standard deviation: (a) AA′ uses both leveling and GPS, (b) BB′ uses leveling, (c) CC′ uses GPS measurements, (d) DD′ uses leveling and (e) EE′ shows groundwater depth. Locations of faults are indicated with grey columns, locations of fissures are indicated with vertical dashed lines in each panel, topography is shown on the bottom and the height scale is indicated with the right inner axis. Besides, ground water depth is indicated with the right outer axis in panel (e).

active fissures including f1, f5, f11, f13, f14, f15 and f17 during the SAR monitoring period are consistent with the land subsidence deformation.

7. Discussion

7.1. Long-term, slow-rate movement of Zhongtiaoshan fault (ZTF)

Within the Yuncheng sub-basin, the ZTF can be classified into a Xiaxian segment (northern segment, with a northeast trend), a Haizhou segment (central segment, with a north-northeast trend) and a Hanyang segment (southern segment, with a northeast trend) according to the geometric discontinuity of the fault strike (Cheng and Yang, 2002). As both the northern and southern segments are relatively weaker and the recurrence intervals of large earthquakes are long (Cheng and Yang, 2002), we mainly focus on the central, Haizhou, segment. The three profiles CC′, DD′ and EE′ in Fig. 5 cross the central segment of ZTF. All leveling, GPS and InSAR results show the ZTF has around 2 mm/yr vertical displacement.

The fault displacement can also be estimated from the displacement of terraces, alluvial fans and other planes (Hetzel et al., 2002; Ran et al., 2010). For a quantitative estimate of medium- and long-term fault displacement, identification of the same geological unit on both sides of the fault provides a good benchmark. If we can determine the exact age of the same depositional unit, it is possible to calculate the mean slip rate of the fault (Ran et al., 2002). Comparison of previous surfaces buried at depth using the ^{14}C age is an optimal method and has a high accuracy. Employing ^{14}C dating, specific gravel layers in the uplifted side can be correlated to gravel on the downthrown side. A trench located near Haizhou in middle section reveals that the cumulative vertical displacements are as large as 18.4 ± 1 m and the mean slip rate is 0.75 ± 0.05 mm/yr since 24.7 ka BP (Si et al., 2014). InSAR results indicate the fault slip rate twice that of the ^{14}C dating results. The difference can be explained as the difference between the influence belt of faults (as wide as 1–10 km) and the measurement length of the trench (as short as tens meters) to date the same layer.

7.2. Land subsidence mechanism

The excessive exploitation of groundwater caused land subsidence in Yuncheng sub-basin, but the spatial pattern of land subsidence is not only controlled by groundwater withdrawal; it is also affected by formation characteristics and geological structures. From Fig. 5, the land subsidence regions are mainly located in the alluvial plain, which are controlled by surrounding normal faults. The different magnitudes of land subsidence in spatial domain are likely attributable to the differing thickness and hydraulic properties of the aquifers and aquitards underlying these areas.

Yuncheng sub-basin is an alluvial and lacustrine deposition plain, so all upper, middle and lower Pleistocene series are the main underground water exploitation strata. Fig. 8 depicts the Hydrostratigraphic section along the same line CC′ from Figs. 5 and 6(c). Gushan on the Emei tableland is composed primarily of clastic rock and Zhongtiao Mount is principally metamorphic rock. Thus, underground water related deformation has no effect on the uplift of the two tablelands on the foot walls of two normal faults, as discussed before, and the 2 mm/yr uplift of those tablelands can be explained as the long-term interseismic fault movement.

Further, the basin-scale land subsidence can be explained as the consolidation of the aquifer system, as land subsidence has close correlation to the pore water in unconsolidated formation. Underground water logs indicate that two wells (W-1 and W-2) along profile CC′ have experienced the different confined water level changes from 2006 to 2011. At well W-1 in Fig. 8, 12 m water level declines at the depth around 150 m, while at well W-2, 4 m water level declines at the depth

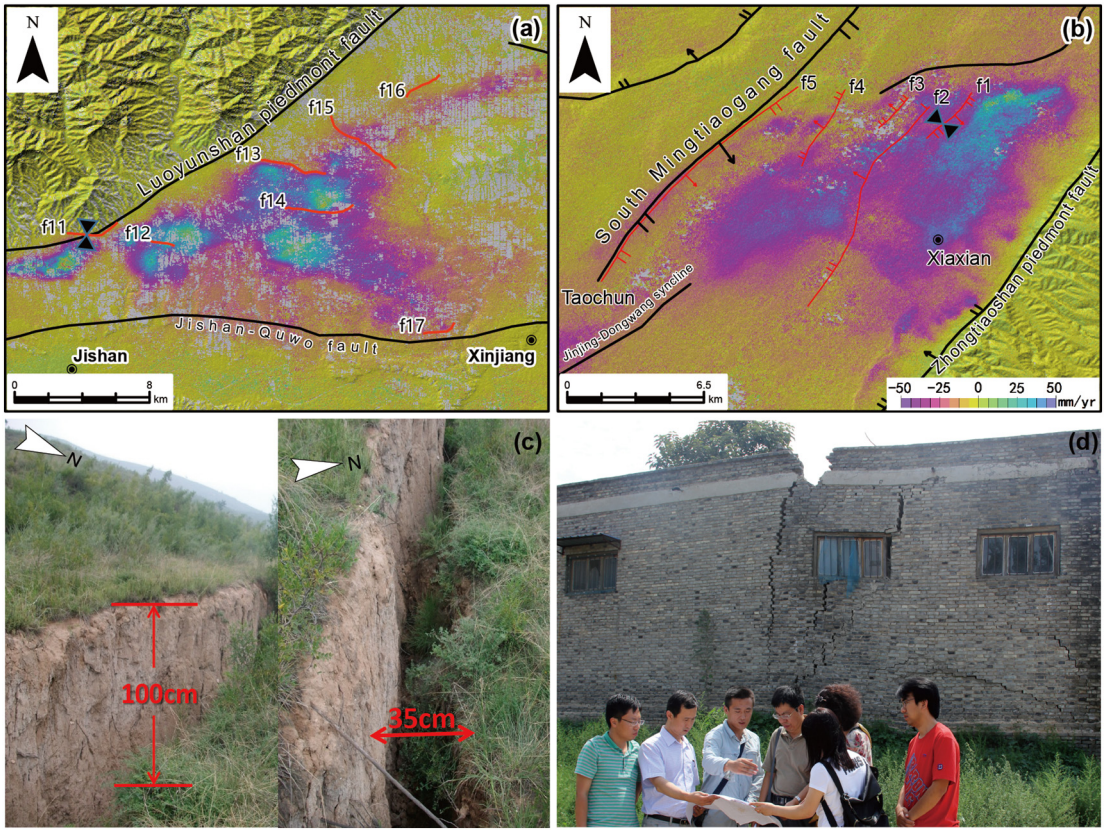

Fig. 7. Two enlarged deformation maps over (a) Jishan in Linfen sub-basin and (b) Xiaxian in Yuncheng sub-basin. Faults (black lines) and local fissures (red lines) are superimposed on. (c) Field photos on f11 in panel (a), and (d) damaged house photo on f1 in panel (b). Two pair of triangles in both panel (a) and (b) indicate the places where the photos were taken. (For interpretation of the references to colour in this figure legend, the reader is referred to the web version of this article.)

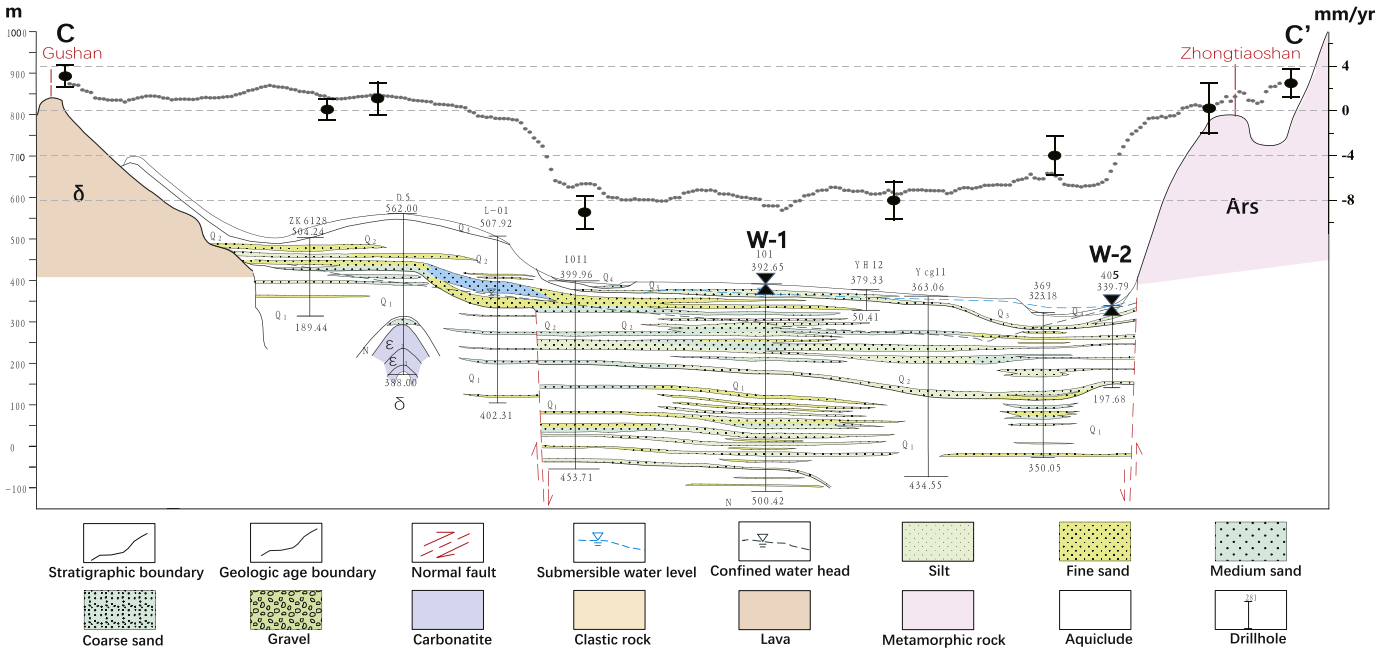

Fig. 8. Hydrostratigraphic section along the line CC′, the top curve is the deformation measured by InSAR and leveling same as the one in Fig. 6(c) (after Meng, 2011). W-1 and W-2 are two wells to monitor the ground water changes. (For interpretation of the references to colour in this figure legend, the reader is referred to the web version of this article.)

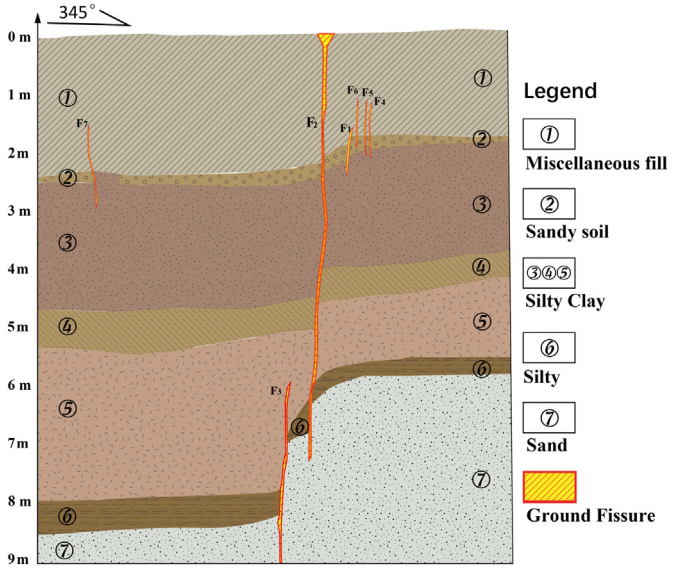

Fig. 9. Profile of trench of fissure f1 in Xiaxian County in Yuncheng sub-basin in Fig. 7(b) (after Liu, 2014). (For interpretation of the references to colour in this figure legend, the reader is referred to the web version of this article.)

around 20 m (Meng, 2011). On the other hand, the clay interlayers at well W-1 are greater in number and the individual interlayers are thinner than at well W-2. When there are many thin clay interlayers in the deposits, water can be drained off through both sides and/or in different directions (Ma et al., 2006). Consequently, as the groundwater head declines, the clay interlayers drain relatively quickly, resulting in proportionately greater subsidence.

7.3. Ground fissure mechanism

As shown in Fig. 7(a) and (b), the ground fissures occur between two normal faults and in the segment with large spatial gradient in land subsidence. The profile of the trench of the fissure f1 in Fig. 7(b) is shown in Fig. 9. We can see cluster fissures occur surrounding one main fissure F_2 on both sides. The main fissure ruptured to the surface with a depth exceeding 7 m, while others are still buried in the subsurface, but formed between two or three different clay layers. From Fig. 9, it is clearly to see the deeper the layer, the larger dislocation, which can be inferred that the mechanism of ground fissure is the upward extension of deep-seated fault. Moreover, the research region is located within the intensive underground water withdrawal area, where the water extraction intensity is up to 1–1.5 million $m^3/km^2/yr$ (Geological Environmental Monitoring Center in Shanxi Province, 2013), where deep phreatic water at lower Pleistocene stratum was mainly exploited. Therefore the formation of ground fissure(s) in this region can be explained as vertical compaction of soil with different compaction rates at different clay layers caused by the underground water declines. This is consistent with similar observations and interpretations reported in the past (Helm, 1994; Burbey, 2002; Bell et al., 2008; Galloway et al., 1998).

8. Conclusions

The Linfen-Yuncheng basin, a region with complex surface deformation phenomena, presents an opportunity to study the different scales of deformation fields and their mechanisms. The following conclusions can be summarized:

1) For long-term and slow-rate basin scale deformation monitoring, Π-RATE InSAR method is a good technique, due to its success in reducing atmospheric effect and orbital errors, and its robust phase unwrapping error detection.
2) Basin-range scale surface deformation maps can be well achieved by combining multiple SAR data. InSAR accuracy is around 3 mm/yr.
3) Three tablelands, namely Luoyun Mount, Emei tableland and Zhongtiao Mount in LYB are all displaying uplift with a magnitude of around 2 mm/yr. Five normal faults with NNE directions in this basin are active during this monitoring period.
4) Land subsidence in both small regions and/or even entire sub-basin regions are precisely monitored with Π-RATE InSAR method, and may be soundly explained as the hydrostratigraphic heterogeneity and varying underground water level changes.
5) Some active ground fissures in the study region have been detected with InSAR. The formation mechanism may be scientifically explained as the joint function of normal fault location, stratum formation and underground water decline.

Acknowledgements

ALOS/PALSAR data are copyrighted by Japan Aerospace Exploration Agency (JAXA) and METI, Envisat data are provided by the European Space Agency (proposal ID. 8140). Three-arc-second SRTM DEM is freely downloaded from http://www2.jpl.nasa.gov/srtm/cbanddataproducts.html. This research is supported by Natural Science Foundation of China (Grant No. 41731066, 41628401, 41874005) and the Special Project of the China Earthquake Administration (No. 2018010103). Π-RATE software are copyrighted by Leeds University. Dr. Meng Lingchao, Qiao Jianwei, Hao Ming and Cui Duxin are appreciated for providing their basic in-situ information. Special thanks go to Chickering Cathy from Southern Methodist University for her intensive reading, checking and constructive comments.

References

Bell, J.W., Amelung, F., Ferretti, A., Bianchi, M., Novali, F., 2008. Permanent scatterer InSAR reveals seasonal and long-term aquifer-system response to groundwater pumping and artificial recharge. Water Resour. Res. 44, 282–288.
Biggs, J., Wright, T., Lu, Z., Parsons, B., 2007. Multi-interferogram method for measuring interseismic deformation: Denali Fault, Alaska. Geophys. J. Int. 170, 1165–1179.
Burbey, T.J., 2002. The influence of faults in basin-fill deposits on land subsidence, Las Vegas Valley, Nevada, USA. Hydrogeol. J. 10, 525–538.
Cheng, S.P., Yang, G.Z., 2002. Late quaternary segmentation model of the Zhongtiaoshan fault, Shanxi province. Seismol. Geol. 24, 289–302.
Cui, D., Hao, M., Li, Y., Wang, W., Qin, S., Li, C., 2016. Present-day crustal movement and strain of the surrounding area of Ordos block derived from repeated GPS observations. Chin. J. Geophys. 59 (10), 3646–3661 (in Chinese).
Elliott, J.R., Biggs, J., Parsons, B., Wright, T.J., 2008. InSAR slip rate determination on the Altyn Tagh Fault, northern Tibet, in the presence of topographically correlated atmospheric delays. Geophys. Res. Lett. 35, 82–90.
Farr, T.G., et al., 2007. The Shuttle Radar Topography Mission. Rev. Geophys. 45, RG2004. https://doi.org/10.1029/2005RG000183.
Ferretti, A., Prati, C., Rocca, F., 2001. Permanent scatterers in SAR interferometry. IEEE Trans. Geosci. Remote Sens. 39, 8–20.
Galloway, D.L., Hudnut, K.W., Ingebritsen, S.E., Phillips, S.P., Peltzer, G., Rogez, F., Rosen, P.A., 1998. Detection of aquifer system compaction and land subsidence using interferometric synthetic aperture radar, Antelope Valley, Mojave Desert, California. Water Resour. Res. 34, 2573–2585.
Garthwaite, M.C., Wang, H., Wright, T.J., 2013. Broadscale interseismic deformation and fault slip rates in the central Tibetan Plateau observed using InSAR. J. Geophys. Res. Solid Earth 118, 5071–5083.
Geological Environmental Monitoring Center in Shanxi Province, 2013. Land Subsidence and Ground Fissures Monitoring Report of Shanxi Basin, 2006. (inner report in Chinese, unpublished).
Hanssen, R.F., 2001. Radar Interferometry: Data Interpretation and Error Analysis. Springer Science & Business Media.
Hao, M., Wang, Q., Shen, Z., Cui, D., Ji, L., Li, Y., Qin, S., 2014. Present day crustal vertical movement inferred from precise leveling data in eastern margin of Tibetan Plateau. Tectonophysics 632, 281–292.
Hao, M., Wang, Q., Cui, D., Liu, L., Zhou, L., 2016. Present-day crustal vertical motion around the Ordos block constrained by precise leveling and GPS data. Surv. Geophys. 37, 923–936.
Helm, D.C., 1994. Horizontal aquifer movement in a Theis-Thiem confined system. Water Resour. Res. 30, 953–964.
Hetzel, R., Niedermann, S., Tao, M., Kubik, P.W., Ivy-Ochs, S., Gao, B., Strecker, M.R., 2002. Low slip rates and long-term preservation of geomorphic features in Central

Asia. Nature 417, 428–432.
Ji, L., Zhang, Y., Wang, Q., Xin, Y., Li, J., 2016. Detecting land uplift associated with enhanced oil recovery using InSAR in the Karamay oil field, Xinjiang, China. Int. J. Remote Sens. 37 (7), 1527–1540. https://doi.org/10.1080/01431161.2016.1154222.
Liu, Y., 2014. The Study on the Mass Mechanism of Ground Fissures in Piedmont Fault on the Plate-case of Yuncheng Basin Xiaxian Ground Fissures. Chang'an University (in Chinese).
Liu, R., Ji, L., 2014. Present-day crustal deformation of Linfen basin and its boundary faults. J. Geodesy Geodyn. 34 (1), 28–31 (in Chinese).
Liu, R., Li, H., Yang, S., 2016. Regional crustal deformation characteristic before 2016 Yuncheng M 4.4 earthquake swarm based on CMONOC continuous GPS data. Geodesy Geodyn. 7 (6), 459–464.
Ma, R., Wang, Y., Ma, T., Sun, Z., Yan, S., 2006. The effect of stratigraphic heterogeneity on areal distribution of land subsidence at Taiyuan, northern China. Environ. Geol. 50, 551–568.
Meng, L., 2011. Study on the Formation Mechanism of Ground Fissures in Shanxi Fault Basin. Chang'an University (in Chinese).
Parker, A.L., Biggs, J., Lu, Z., 2014. Investigating long-term subsidence at Medicine Lake Volcano, CA, using multitemporal InSAR. Geophys. J. Int. 199, 844–859.
Ran, Y., Zhang, P., Hu, B., Guo, W., 2002. Paleoseismic activity on the Hohhot segment of Daqingshan piedmont fault in the Late Quaternary history. In: Earthquake Research in China. vol. 28. pp. 15–27.
Ran, Y., Chen, L., Chen, J., Wang, H., Chen, G., Yin, J., Shi, X., Li, C., Xu, X., 2010. Paleoseismic evidence and repeat time of large earthquakes at three sites along the Longmenshan fault zone. Tectonophysics 491, 141–153.
Si, S., Li, Y., Lü, S., Wang, Y., 2014. Holocene slip rate and paleoearthquake records of the Salt Lake segment of the Northern Zhongtiaoshan Fault, Shanxi Province. Sci. China Earth Sci. 57, 2079–2088.
Walters, R., Parsons, B., Wright, T., 2014. Constraining crustal velocity fields with InSAR for Eastern Turkey: limits to the block-like behavior of Eastern Anatolia. J. Geophys. Res. Solid Earth 119, 5215–5234.
Wang, X., 1995. Recent crustal deformation field and time-space evolution character in Linfen Basin. In: Earthquake Research in Shanxi, (in Chinese).
Wang, H., Wright, T.J., 2012. Satellite geodetic imaging reveals internal deformation of western Tibet. Geophys. Res. Lett. 39, 127–137.
Wang, H., Wright, T.J., Biggs, J., 2009. Interseismic slip rate of the northwestern Xianshuihe fault from InSAR data. Geophys. Res. Lett. 36, 139–145.
Wang, H., Wright, T.J., Yu, Y., Lin, H., Jiang, L., Li, C., Qiu, G., 2012. InSAR reveals coastal subsidence in the Pearl River Delta, China. Geophys. J. Int. 191, 1119–1128.
Yang, C.S., Zhang, Q., Xu, Q., Zhao, C.Y., Peng, J.B., Ji, L.Y., 2016. Complex deformation monitoring over the Linfen–Yuncheng Basin (China) with time series InSAR technology. Remote Sens. 8, 284.